



TECHNICAL ARTICLE

# The Effect of Water Ejection and Rewetting Phenomena on Hot Cracking Sensitivity during Direct Chill Casting of Magnesium Alloy

P.V. Sai Divya, P.K. Penumakala, and A.K. Nallathambi

Submitted: 14 May 2022 / Revised: 5 August 2022 / Accepted: 20 August 2022 / Published online: 20 October 2022

The production of industrial-scale ingots and billets with minimum defects through direct chill (DC) casting process is highly sensitive to casting parameters such as cooling water flow rate and casting speed. For given casting conditions, if the billet attains higher surface temperature, water ejection occurs in secondary cooling zone of DC casting. This affects the temperature distribution during the casting process and associated defects. In the present study, the influence of water ejection phenomenon on thermal stresses and occurrence of hot cracks in DC casting of magnesium alloy was studied using a thermo-mechanical mathematical model. The effect of casting speed and water flow rate on thermal profiles was investigated, and critical casting speed beyond which water ejection phenomenon occurs was established for AZ31 magnesium alloy. Detailed studies were carried out for two different cases of complete and delayed wetting (ejection followed by wetting). Results indicated that tensile stresses were high in the impingement region for complete wetting. For delayed wetting, peak tensile stresses were observed at the bottom of the billet immediately after rewetting. Hot tearing studies based on (Rappaz–Drezet–Gremaud) RDG criterion indicated that center of the billet near bottom block was more sensitive to hot cracking in both complete and delayed wetting cases. However, delayed wetting further increased the risk of hot tearing.

**Keywords** DC casting, hot cracking, magnesium alloy, rewetting, secondary cooling, water ejection

## 1. Introduction

Direct chill (DC) casting is a widely used processing method for casting ingots and billets of nonferrous alloys such as aluminum and magnesium. The schematic of DC casting process with different cooling zones is shown in Fig. 1(a). During this process, liquid metal is continuously poured into an open-ended mold, supported by bottom block at its lower end. A solid shell is formed at the mold/bottom block interface due to *primary cooling* by water circulating in the annular area of the mold. When the outer solid shell is able to support the incoming liquid metal, bottom block is lowered with certain speed. The speed at which the bottom block is lowered is referred as casting speed. At the exit of the mold, water jets

The original version of this article was revised: In the article as originally published the author names were not presented as the authors intended. The author list should read “P.V. Sai Divya, P.K. Penumakala, and A.K. Nallathambi”.

**P.V. Sai Divya** and **P.K. Penumakala**, Department of Mechanical Engineering, Birla Institute of Technology and Science-Pilani, Hyderabad Campus, Pilani, India; and **A.K. Nallathambi**, Department of Mechanical Engineering, National Institute of Technology, Tiruchirappalli, India. Contact e-mail: p20160419@hyderabad.bits-pilani.ac.in.

Abbreviations	
DC	Direct chill
RDG	Rappaz–Drezet–Gremaud
IZ	Impingement zone
FFZ	Free-falling zone
BC	Boundary condition
HTC	Heat transfer coefficient
FB	Film boiling
NB	Nucleate boiling
TB	Transition boiling
FC	Forced convection
DNB	Departure from nucleate boiling temperature
List of symbols	
$k$	Thermal conductivity ( $\text{W m}^{-1} \text{K}^{-1}$ )
$T$	Temperature ( $^{\circ}\text{C}$ )
$\rho$	Density ( $\text{kg m}^{-3}$ )
$C_p$	Specific heat capacity ( $\text{J kg}^{-1} \text{K}^{-1}$ )
$\Delta h$	Latent heat ( $\text{J kg}^{-1}$ )
$T_{\text{Liq}}$	Liquidus temperature ( $^{\circ}\text{C}$ )
$T_{\text{sol}}$	Solidus temperature ( $^{\circ}\text{C}$ )
$K$	Thermal conductance matrix
$C$	Capacitance matrix
$L$	Latent heat vector
$F$	Force vector
$T_s$	Surface temperature ( $^{\circ}\text{C}$ )
$T_f$	Cooling water temperature ( $^{\circ}\text{C}$ )
$T_{\text{coh}}$	Coherency temperature ( $^{\circ}\text{C}$ )
$\varnothing_{\text{IZ}}$	Heat flux in the impingement zone ( $\text{W m}^{-2}$ )

$Q$	Volumetric cooling water flow rate per unit of perimeter ( $\text{L min}^{-1} \text{m}^{-1}$ )
$T_{\text{Le}}$	Leidenfrost temperature ( $^{\circ}\text{C}$ )
$e_{\text{th}}$	Thermal effusivity ( $\text{J/m}^2\text{K.s}^{-1/2}$ )
$T_{\text{Re}}$	Rewetting temperature ( $^{\circ}\text{C}$ )
$T_{\text{amb}}$	Ambient temperature ( $^{\circ}\text{C}$ )
$T_{\text{sat}}$	Water saturation temperature ( $^{\circ}\text{C}$ )
$Q_{\text{FFZ}}$	Heat flux in the free-falling zone ( $\text{W m}^{-2}$ )
$T_{\text{ini}}$	Impingement point temperature ( $^{\circ}\text{C}$ )
$S$	Cauchy stress tensor
$b_f$	Body force vector
$(t_f)$	Traction force vector
$E$	Total strain tensor
$E_e$	Elastic strain tensor
$E_{\text{th}}$	Thermal strain tensor
$E_{\text{ie}}$	Inelastic strain tensor
$\alpha$	Coefficient of thermal expansion
$U$	Displacement vector
$f_s$	Solid fraction

strike the surface of the billet further reducing its temperature. This constitutes *secondary cooling*. Heat transfer across the billet and bottom block interface constitutes the *bottom block cooling*. Further, this process is divided into three phases based on the temperature profiles: start-up, pseudo-steady-state and end phases. Start-up phase is the most critical phase prone to defects such as cracks. This is due to conglomerative effect of primary, secondary and bottom block cooling. Caron and Wells (Ref 1) emphasized that secondary cooling is the most critical region owing to maximum heat extraction due to direct contact of water with the billet.

Secondary cooling region comprises of impingement zone (IZ) in which water strikes the surface of billet and free-falling zone (FFZ) where water flows down the billet surface. As shown in Fig. 1(b), when cooling water strikes the billet surface, film boiling occurs due to the formation of vapor film, if surface temperature of the billet is higher than the Leidenfrost temperature (Ref 2). This impingement zone (IZ) is critical to heat transfer as vapor film acts as an insulator preventing the cooling water from wetting the billet surface. Caron and Wells (Ref 3) proposed a relation between water flow rate and IZ length. In most cases, IZ length is approximately 10 to 15 mm based on water flow rate (Ref 4). It is to be noted that if the jet horizontal momentum is high enough, vapor film may break and cause wetting. Below IZ, i.e., in free-falling zone (FFZ), if surface temperature is still above the Leidenfrost temperature, cooling water is ejected away from the surface due to the absence of jet's horizontal momentum to oppose the vapor film. However, as cooling progresses, if surface temperature falls below a critical temperature called rewetting temperature, water again contacts the surface. The rewetting front propagates down the billet surface with further cooling. Caron and Wells (Ref 3) expressed the Leidenfrost temperature and rewetting temperature as functions of water flow rate. Further, Kulkarni (Ref 4) studied the influence of billet surface condition and water jet angle on wetting front propagation. Defects that arise in DC casting are highly sensitive to the mechanism of heat transfer in secondary cooling zone.

Numerical modeling of DC casting is used to analyze the effect of various process parameters and casting conditions on

evolution of temperature and stress profiles. Heat transfer boundary conditions in secondary cooling region are crucial in determining temperature distribution at various stages of casting process. Earlier studies used nonlinear boiling curves to account for different boiling heat transfer phenomenon observed in secondary cooling zone. Based on quenching experiments on AZ31 plate, Caron and Wells (Ref 1) proposed empirical relations for heat flux as a function of cooling water flow rate, plate surface temperature and plate initial temperature for both IZ and FFZ. Sai Divya et al. (Ref 5) used nonlinear boiling curves in secondary cooling region to estimate the temperature profiles during the DC casting of magnesium alloys and analyzed the effect of positioning the wiper on the temperature distribution. Caron and Wells (Ref 6) analyzed the effect of various casting parameters such as casting speed, flow rate and impingement point temperature on boiling curves by conducting cooling tests on AA5182 plates. Bolduc and Kiss (Ref 7) conducted sensitivity studies to analyze the importance of boiling parameters on sump depth, solidified shell thickness and ingot base temperature.

Based on numerically estimated temperature profiles, few works were dedicated to the study of water ejection phenomena in DC casting. Sengupta et al. (Ref 8) used 2D transient heat transfer model to study the influence of water ejection in aluminum DC casting. Boundary conditions used in their study were dependent on water flow rate, surface temperature and impingement point temperature. The sensitivity of casting and material parameters on temperature profiles and water ejection was analyzed. Sengupta et al. (Ref 9) studied the temperature variation at various positions across the ingot with and without water ejection phenomenon during DC casting of AA5182 ingots. It was emphasized that stable film boiling on the ingot surface causes water ejection resulting in high ingot temperatures below the stable ejection front. Boiling curves used in the model were functions of surface temperature, water flow rate and distance from the water impingement point. Caron and Wells (Ref 3) reported that film boiling can be observed only in the impingement zone where horizontal momentum of jet compensates the pressure developed by the vapor formation. In the free-falling region, the absence of opposing force to vapor pressure causes water ejection, and hence, stable film boiling is not observed. Further, they investigated the effect of various casting parameters on water ejection phenomenon and developed a correlation between water flow rate and critical casting speed which results in water ejection. It was concluded that high casting speeds and low flow rates together with high thermal effusivity of the material were favorable conditions for water ejection.

Prediction of thermal strains and stresses is essential to analyze the formation of various surface and subsurface cracks during casting process. Few works reported various thermo-mechanical models required to estimate the evolution of thermal stresses in DC Casting. Material behavior at high temperatures is key input for mechanical models of DC casting. Hao et al. (Ref 10) developed a thermal stress numerical model in ABAQUS using elastic rate-independent plastic constitutive model to analyze thermal stresses in AZ31 alloy DC casting. Turski et al. (Ref 11) predicted thermal stress profiles in DC casting of high strength WE43 magnesium alloy slabs. Drezet and Pirling (Ref 12) studied thermo-mechanical behavior during DC casting process of AA7050 ingots. Hongjun et al. (Ref 13) analyzed thermal stresses and strains in DC casting of AZ31alloy and studied the effect of casting parameters on

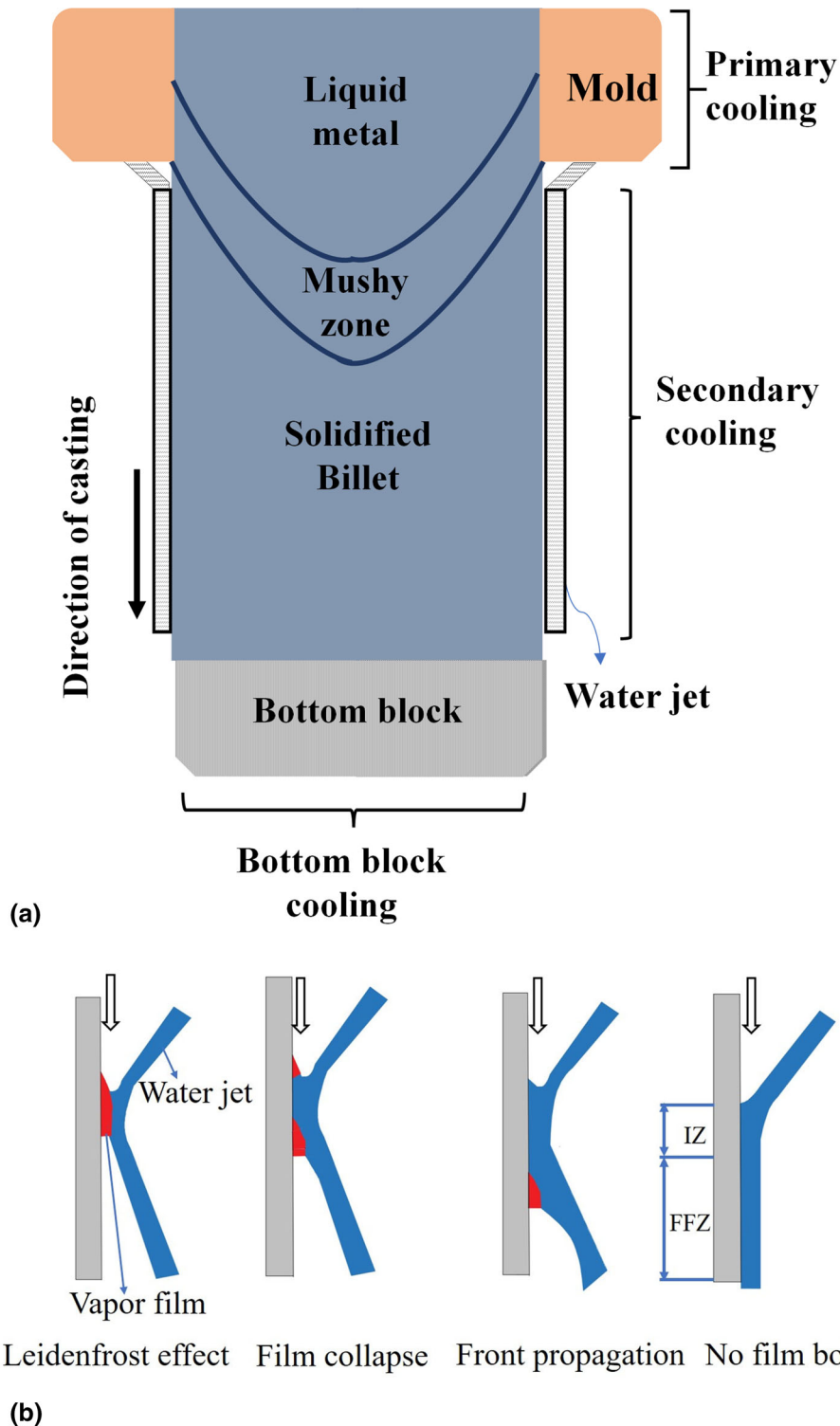


**Fig. 1** Schematic of (a) DC casting and (b) water ejection followed by front propagation and complete wetting

temperature and stress profiles. Suyitno et al. (Ref 14) carried out thermal and mechanical study for a DC cast Al 4.5% Cu alloy using rate-dependent constitutive model. Menapace et al. (Ref 15) used rate-dependent constitutive model to express constitutive behavior of a DC cast AA6082 Al alloy. Recently, Kulkarni (Ref 4) and Ramasamy (Ref 16) have investigated the

effect of water ejection on thermal stress profiles in DC casting. Thermo-mechanical studies for three different surface conditions were carried out: Hot casting (water ejection), cold casting (complete wetting) and delayed wetting (ejection followed by wetting). In case of cold casting, surface cracks were generated at the impingement point due to high tensile stresses that

propagated towards the bottom of the ingot resulting in failure of entire ingot. In case of delayed wetting, susceptibility for occurrence of cracks was high near the bottom of the ingot due to wetting front collapse and propagation. Sengupta et al. (Ref 17) studied the stress and strain variations for both cold and hot cast conditions. Thermal stresses were compared for both cases and highlighted the need for hot tearing criterion to evaluate the susceptibility to cracking.

The output from thermo-mechanical models is used to predict the formation of hot tears using various criteria. Grandfield et al. (Ref 18) reported that hot tears/cracks develop during start-up phase in mushy zone when solid fraction is close to 1. Mechanism of hot tear formation was studied extensively for aluminum alloy DC casting. Eskin et al. (Ref 19) reviewed various hot cracking criterion and classified them into mechanical and non-mechanical criterion. Mechanical criteria are based on stresses and strains (Ref 20), whereas non-mechanical criteria are based on temperature evolution during the casting process. Suyitno et al. (Ref 21) implemented different mechanical and non-mechanical hot tearing criterion in DC casting of Al 4.5% Cu alloy and compared hot tearing sensitivity in the billet. Among various criteria, RDG criterion was found to be suitable in estimating hot tearing sensitivity for different processing conditions. Several material parameters such as fracture strain and critical pressure drop in the mushy zone are to be known a priori for using these hot tearing criteria. However, obtaining these parameters for magnesium alloy casting is very difficult. Bichler et al. (Ref 22) predicted minimum stress and strain conditions for hot cracks formation in AZ91D magnesium alloy casting. Song et al. (Ref 23) summarized various hot tearing criterion for magnesium alloys which are valid in case of static casting. Studies on implementing different hot tearing criteria for magnesium alloy DC casting are still limited.

Secondary cooling has major influence on wetting/ejection phenomenon during the start-up phase of DC casting (Ref 1–3, 9, 17). Secondary cooling depends on various process parameters such as flow rate, casting speed, impingement point temperature, rewetting temperature and thermal effusivity of the material. Water ejection increases the susceptibility for the formation of hot cracks as billet remains in mushy zone for longer period of time. Even though few works (Ref 9) predicted temperature profiles during water ejection, numerical studies on thermal stress and hot cracking investigations for DC casting of Mg alloys do not exist in the literature. To critically analyze the effect of water ejection and delayed wetting on billet quality, there is a necessity to implement a suitable hot tearing criteria in addition to stress analysis.

The present work is focused on presenting detailed thermo-mechanical analysis and hot cracking aspects of magnesium alloy DC casting. In this regard, thermo-mechanical analysis was carried out for two different cases: one with complete wetting and other with water ejection followed by wetting (delayed wetting) in FFZ zone. The effect of these two conditions on thermal stress profiles is presented. Further, susceptibility of the billet to hot cracks is analyzed by implementing RDG criterion, a strain rate-based hot tearing criterion, developed by Rappaz et al. (Ref 24). This criterion is based on the calculation of depression pressure in the mushy zone. The influence of two critical parameters, i.e., water flow rate and casting speed, on secondary cooling is studied. A relation has been developed to determine the critical casting

speed which defines the speed above which water ejection takes place.

## 2. Modeling of DC Casting Process

DC casting process is replicated by a numerical model using an in-house code developed in MATLAB. An axis-symmetric billet of radius 227.5 mm is modeled using boundary conditions (BC) shown in Fig. 2. In actual process, the mold remains stationary while billet and bottom block move down with the casting speed. However, the process is replicated in this work by fixing the billet, bottom block and moving the mold vertically upwards with the casting speed. The feeding of the liquid metal from the top is modeled by adding new layer of computational domain at each time step.

### 2.1 Thermal Model

The general 2D heat conduction equation in cylindrical coordinates with modified specific heat term considering latent heat release is given in Eq 1.

$$\frac{1}{r} \frac{\partial}{\partial r} \left( kr \frac{\partial T}{\partial r} \right) + \frac{\partial}{\partial z} \left( k \frac{\partial T}{\partial z} \right) = \rho \left( C_p + \frac{\Delta h \partial f_i}{\partial T} \right) \frac{\partial T}{\partial t} \quad (\text{Eq 1})$$

where  $k$  is thermal conductivity,  $T$  is temperature,  $\rho$  is density,  $C_p$  is specific heat,  $\Delta h$  is latent heat,  $f_i$  is the phase fraction, and  $r$  and  $z$  are coordinate directions. Using finite element method (FEM), Eq 1 is converted into weak form, which is expressed in Eq 2

$$\begin{aligned} \int [\nabla \tilde{T} \cdot (k \nabla T)] d\Omega + \int \rho C_p \tilde{T} \dot{T} d\Omega + \int \rho \Delta h \frac{df_i}{dt} \tilde{T} d\Omega + \int h \tilde{T} T d\Gamma \\ = \int h T_\infty \tilde{T} d\Gamma + \int q \tilde{T} d\Gamma \end{aligned} \quad (\text{Eq 2})$$

The weak form is discretized following standard finite element procedure to derive element matrices and force vector as given below,

$$\begin{aligned} K_e &= \int B k B^T d\Omega_e + \int h N N^T d\Gamma_e \\ C_e &= \int \rho C_p N N^T d\Omega_e \\ L_e &= \int N \rho \Delta h f_i d\Omega_e \\ F_e &= \int N h T_\infty d\Gamma_e + \int N q d\Gamma_e \end{aligned} \quad (\text{Eq 3})$$

Using element connectivity matrices, the global matrices and vectors are obtained. The final form of the equation is

$$K \Theta + C \dot{\Theta} + \dot{L} = F \quad (\text{Eq 4})$$

where  $K$  is thermal conductance matrix,  $C$  is capacitance matrix,  $L$  is latent heat vector,  $F$  is global force vector and  $\Theta$  is the nodal temperature vector. Euler explicit scheme used by pavan kumar et al. (Ref 25) for solving the FE-based time-dependent equations is implemented in the present study.

As described in Fig. 2, insulated BC is imposed along the axis of symmetry (BC 1). This BC evolves along with the billet growth. Nodal temperatures along BC 2 are fixed to melt temperature at each time step. In primary (mold) cooling, billet is cooled with the help of water circulating inside the mold. Initially, heat transfer is high at the mold/billet interface as good contact exists between both mold and billet. As cooling

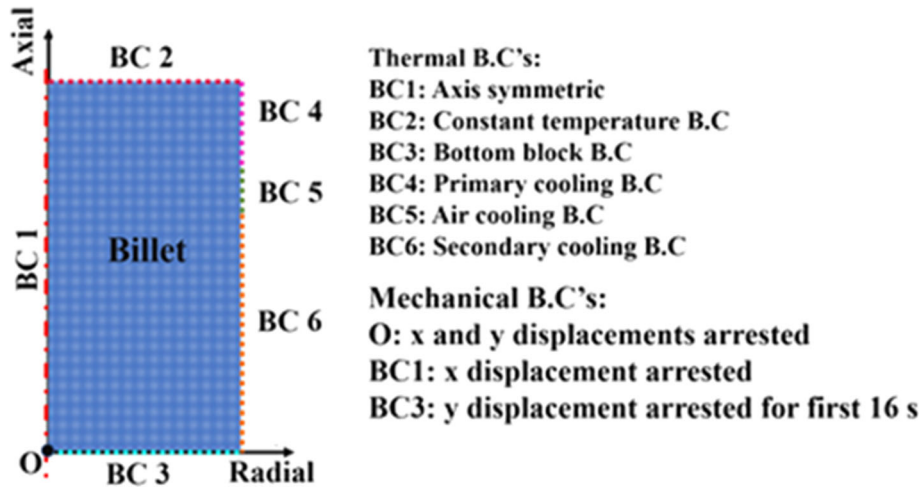


Fig. 2 Computational domain with thermal and mechanical boundary conditions

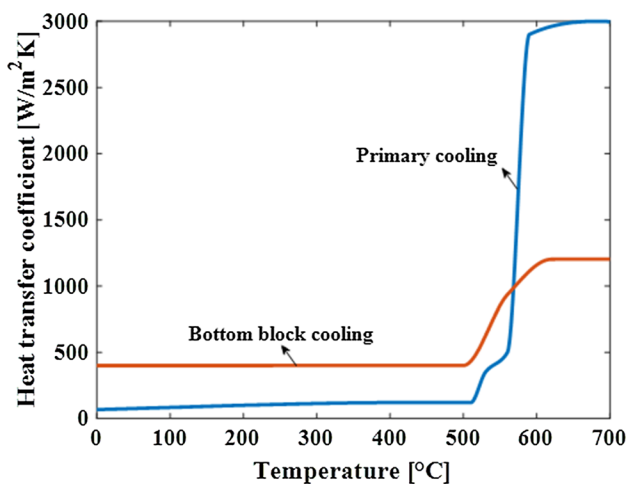
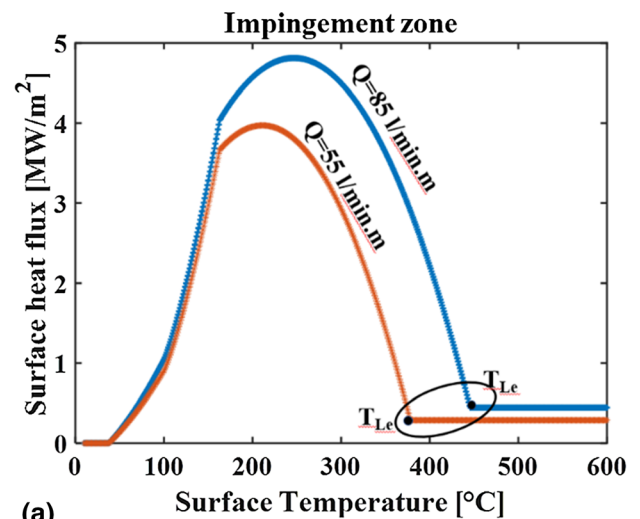


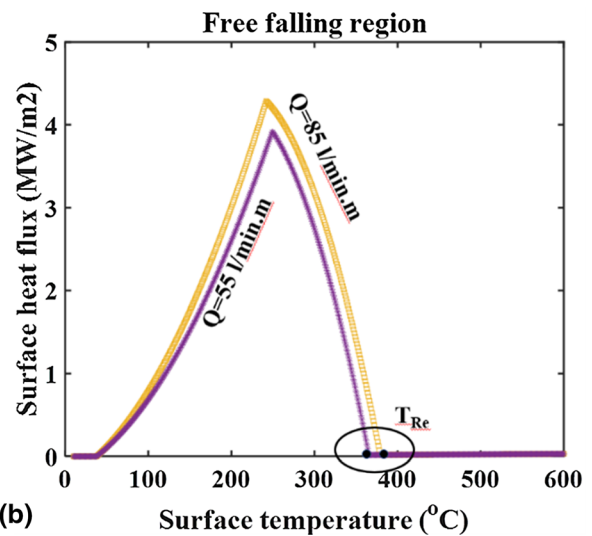
Fig. 3 Variation of primary and bottom block cooling heat transfer coefficient as a function of billet surface temperature

progresses, air gap is created at the billet mold interface due to solidification and shrinkage of molten metal. This leads to a reduction in heat transfer at the mold exit. Along BC4, convective heat transfer boundary conditions are assumed. In this zone, the heat transfer coefficient (HTC) is considered to be a function of temperature. As shown in Fig. 3, HTC decreases with decrease in temperature to account for reduction in heat transfer with solid shrinkage. Similarly, in the bottom block cooling zone, temperature-dependent HTC implemented by Hao et al. (Ref 26) is considered and represented as BC 3 in Fig. 2.

Between the mold exit and impingement zone, small region of the billet experiences air cooling and is shown as BC5 in Fig. 2. A constant HTC of 10 W/m<sup>2</sup>K is considered in this region. Nonlinear boiling curves are used to quantify the heat flux in IZ and FFZ which constitutes the secondary cooling (BC6). These curves represent different boiling regimes such as film boiling, transient boiling and nucleate boiling. Caron and Wells (Ref 3) developed empirical relations for heat flux as function of impingement point and rewetting temperatures in IZ and FFZ, respectively, and these relations are used in the present analysis.



(a)



(b)

Fig. 4 Boiling curves in (a) impingement zone (IZ), (b) free-falling zone (FFZ)

These boiling curves are also highly sensitive to water flow rate, Leidenfrost temperature and rewetting temperature. Figure 4 shows boiling curves in two regions as a function of water flow rate. Leidenfrost temperature ( $T_{Le}$ ) and rewetting temperature ( $T_{Re}$ ) are functions of cooling water flow rate as shown in Fig. 4(a) and (b) (Ref 3). In IZ, if the impingement point temperature ( $T_{ini}$ )  $<$   $T_{Le}$ , complete wetting takes place and heat transfer occurs by transition followed by nucleate boiling. However, if  $T_{ini} > T_{Le}$ , film boiling occurs in IZ and air cooling occurs in FFZ. This is due to the absence of opposing force to press the vapor film against the billet surface in IZ and subsequent water ejection in FFZ. Further, as the surface temperature drops below  $T_{Re}$ , water rewets the surface in FFZ.  $T_{Re}$  is a function of  $T_{ini}$  and controls the propagation of wetting front in FFZ. As  $T_{ini}$  varies with the growth of the billet, a subroutine is developed for dynamically calculating the heat flux based on  $T_{ini}$  in each time step.

## 2.2 Mechanical Model

The thermal stress field was estimated by solving the momentum equation,

$$\nabla \cdot S + \vec{b}_f = \vec{0} \quad (\text{Eq 5})$$

subject to mechanical boundary conditions (BC),

$$\vec{u} = \vec{u}_s; S \cdot \vec{n} = \vec{t}_f \quad (\text{Eq 6})$$

where  $S$  is the Cauchy stress tensor,  $\vec{b}_f$  is the body force vector. Body forces were neglected in the present analysis. In the BCs,  $\vec{u}_s$  is the prescribed displacement vector and  $\vec{t}_f$  is the prescribed traction vector. As per the small deformation theory, the total strain is given by

$$E = E_e + E_{th} + E_{ie} \quad (\text{Eq 7})$$

where  $E_e$  is the elastic strain tensor,  $E_{th}$  is the thermal strain tensor and  $E_{ie}$  is the inelastic strain tensor. Thermal strain ( $E_{th}$ ) is determined by using linearized coefficient of thermal expansion ( $\alpha$ ) using Eq 8,

$$E_{th} = \alpha(T - T_{ref})I \quad (\text{Eq 8})$$

where  $T_{ref}$  is the reference temperature where thermal strain is zero. At high temperatures, as the influence of strain rate is significant on deformation behavior, visco-plastic models such as Norton–Hoff law (in the temperature range,  $T_{sol} < T < T_{coh}$ ) and Garofalo law (for temperatures less than  $T_{sol}$ ) are used for modeling inelastic strains. Here,  $T_{sol}$  is the solidus temperature and  $T_{coh}$  is the temperature of certain point in the mushy zone, where semisolid attains the strength. Norton–Hoff law in the form of Eq 9 implemented by Pavan Kumar et al. (Ref 25) is used in the present study.

$$\dot{\epsilon}^{vp} = \tilde{k} \left( \frac{\sigma_{eff}}{\sigma_0} \right)^n \quad (\text{Eq 9})$$

where  $\dot{\epsilon}^{vp}$  is the equivalent visco-plastic strain rate,  $\sigma_{eff}$  is the von Mises equivalent stress and  $\tilde{k}$ ,  $\sigma_0$  and  $n$  are temperature-dependent constants. Semisolid tensile test data reported by Hu et al. (Ref 27) are used for deriving constants in Eq 9. For the constitutive behavior in solid state, Garofalo law in the form of Eq 10 by Li et al. (Ref 28) is used in the present study.

$$\dot{\epsilon}^{vp} = A \left[ \sinh \frac{\sigma_{eff}}{\sigma_0} \right]^n e^{-\left(\frac{Q}{RT}\right)} \quad (\text{Eq 10})$$

where  $A$ ,  $\sigma_0$  and  $n$  are material-dependent constants.  $Q$  is the activation energy,  $R$  is the universal gas constant and  $T$  is the absolute temperature. The constants were determined by conducting hot tension tests on AZ31 at temperatures ranging from room temperature 30 to 450 °C at three strain rates 0.001 s<sup>-1</sup>, 0.01 s<sup>-1</sup> and 0.1 s<sup>-1</sup>. The momentum equation (Eq 5) is solved using FEM. For any displacement field  $\vec{u}$ , Eq 5 is integrated resulting in the following weak form, expressed as follows

$$\int S : \tilde{E} d\Omega = \int \vec{t}_f \cdot \vec{u} d\Gamma + \int \vec{b}_f \cdot \vec{u} d\Omega \quad (\text{Eq 11})$$

Using standard FEM procedure, final form is given as,

$$KU = F \quad (\text{Eq 12})$$

where  $K$  is the stiffness matrix,  $F$  is the force vector and  $U$  is the displacement vector. Newton–Raphson method elucidated by Pavan Kumar et al. (Ref 25) for solving rate-dependent constitutive equations in Eq 9 and 10 is used in the present study. The entire algorithm is developed in MATLAB. The mechanical BC used to model the DC casting is depicted in Fig. 2. Along the axis of symmetry, displacement is restricted in x direction. At the node located at ‘O,’ both x and y displacements are arrested. At bottom of the billet, y displacement is arrested initially and then released, to avoid penetration of billet into the bottom block. Thermo-physical properties (thermal conductivity, specific heat and density) are given in Table 1. Figure 5 shows nonlinear phase fraction curve, elastic modulus and coefficient of thermal expansion.

## 2.3 Implementing RDG Hot Cracking Criterion

The RDG criterion presumes that hot tears are prone to occur when pressure in the inter-dendritic regions drops below a critical value during solidification. This pressure drop in the inter-dendritic region occurs because of volumetric change due to both solidification shrinkage ( $\Delta P_{shrinkage}$ ) and mechanical deformation ( $\Delta P_{mech}$ ). This necessitates for an increase/decrease in the liquid metal flow resulting in a pressure drop ( $\Delta P_{mech}$ ). Rappaz et al. (Ref 24) reported that, when the dendritic network is coherent, these stresses get transmitted through the network. When the local temperature is above the coherency point, dendrite arms in the impermeable mushy zone are pulled apart, and if the liquid flow is insufficient to fill this region, opening of the inter-dendritic network results in the formation of hot tears. The pressure drop in the mushy zone can be expressed as follows:

$$P_{mush} = P_{met} - (\Delta P_{shrinkage} + \Delta P_{mech}) \quad (\text{Eq 13})$$

where  $P_{met}$  is the metallostatic pressure. The term  $\Delta P_{shrinkage}$  refers to the pressure drop due to shrinkage and  $\Delta P_{mech}$  refers to the pressure drop due to mechanical deformation. Hot tears will occur when  $P_{mush} < P_{cri}$  (critical pressure). Since the value of this critical pressure is unknown and difficult to obtain experimentally, the present work considers the total pressure drop ( $\Delta P_{shrinkage} + \Delta P_{mech}$ ) for assessing the hot tearing susceptibility. Any location with higher pressure drop is considered to be more susceptible to hot tearing.

**Table 1** Thermo-physical properties used in the numerical model (Ref 29)

Thermal conductivity		Specific heat		Density $\rho$ [kg/m <sup>3</sup> ]	Latent heat $\Delta h$ [kJ/kg]
$T$ [°C]	$k$ [W/m <sup>2</sup> K]	$T$ [°C]	$C_p$ [J/kg K]		
20	76.9	20	1040	1780	339
50	83.9	100	1042		
100	87.3	300	1148		
150	92.4	> 610	1414		
200	97				
250	101.8				
424	118.5				
630	60				
635	120				
680	240				

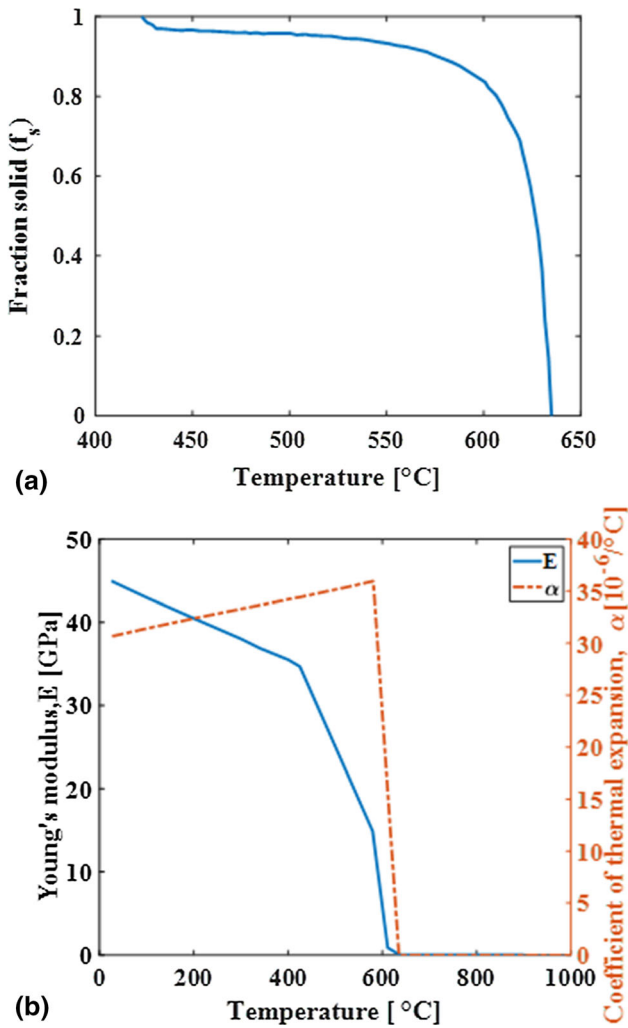


**Fig. 5** Variation of (a) solid fraction and (b) Young's modulus, coefficient of thermal expansion with temperature (Ref 10)

Figure 6(a) shows a small volume element in the mushy zone over which mass balance is performed to calculate the pressure drop. It is assumed that liquid flows along  $x$  direction (direction of heat flow) and solid deforms along  $y$  direction (perpendicular to the direction of heat flow). The mass balance reported by Rappaz et al. (Ref 24) is expressed as,

$$\frac{\partial}{\partial t}(\rho_l f_l + \rho_s f_s) + \frac{\partial}{\partial x}(\rho_l f_l v_{l,x}) + \frac{\partial}{\partial y}(\rho_s f_s v_{s,y}) = 0 \quad (\text{Eq 14})$$

where  $\rho_l$  and  $\rho_s$  are the densities of liquid and solid phases and  $f_l$  and  $f_s$  represent liquid and solid phase fractions, respectively. The term  $v_{l,x}$  denotes velocity of the liquid along the  $x$  direction and  $v_{s,y}$  denotes velocity of the solid along the  $y$  direction. Following the Darcy equation, the liquid and solid velocities can be related to pressure drop. Substituting this in Eq 14, the total pressure drop across the mushy zone is given by

$$(\Delta P_{sh} + \Delta P_{mech}) = \beta \mu \alpha L \int \frac{F}{K} dx + (1 + \beta) \mu \alpha L \int \frac{E}{K} dx \quad (\text{Eq 15})$$

where  $\beta$  is the shrinkage factor =  $\left(\frac{\rho_s}{\rho_l}\right) - 1$  and  $\mu$  is the dynamic viscosity of the liquid. The Kozeny–Carmen relation can be expressed as

$$K = \frac{\lambda_2^2 (1 - f_s)^3}{180 f_s^2} \quad (\text{Eq 16})$$

where  $\lambda_2$  is secondary dendrite arm spacing. The terms  $E$  and  $F$  can be calculated as

$$E = \int_0^x f_s \dot{\epsilon}_p dx \quad (\text{Eq 17})$$

$$F = \int_0^x \frac{df_s}{dt} dx \quad (\text{Eq 18})$$

where  $\dot{\epsilon}_p = \frac{dv_{s,y}}{dy}$  is the strain rate in the solid along the  $y$  direction (perpendicular to the direction of heat flow). This strain rate can be calculated as

$$\dot{\epsilon}_p = \dot{\epsilon}_{p,r} \sin \gamma - \dot{\epsilon}_{p,z} \cos \gamma + \dot{\epsilon}_{p,\theta} \quad (\text{Eq 19})$$

where  $\dot{\epsilon}_{p,r}$ ,  $\dot{\epsilon}_{p,z}$  and  $\dot{\epsilon}_{p,\theta}$  are the radial, axial and circumferential components of strain rate. The variable  $\gamma$  is angle between the thermal gradient line and radial axis, as shown in Fig. 6(b).

In the current work, a subroutine is developed in MATLAB for implementing RDG criterion. Key input parameters like plastic strain rate perpendicular to heat flow ( $\dot{\epsilon}_p$ ), solid fraction ( $f_s$ ), slope of  $f_s$  vs temperature curve ( $\frac{df_s}{dT}$ ) and rate of change of

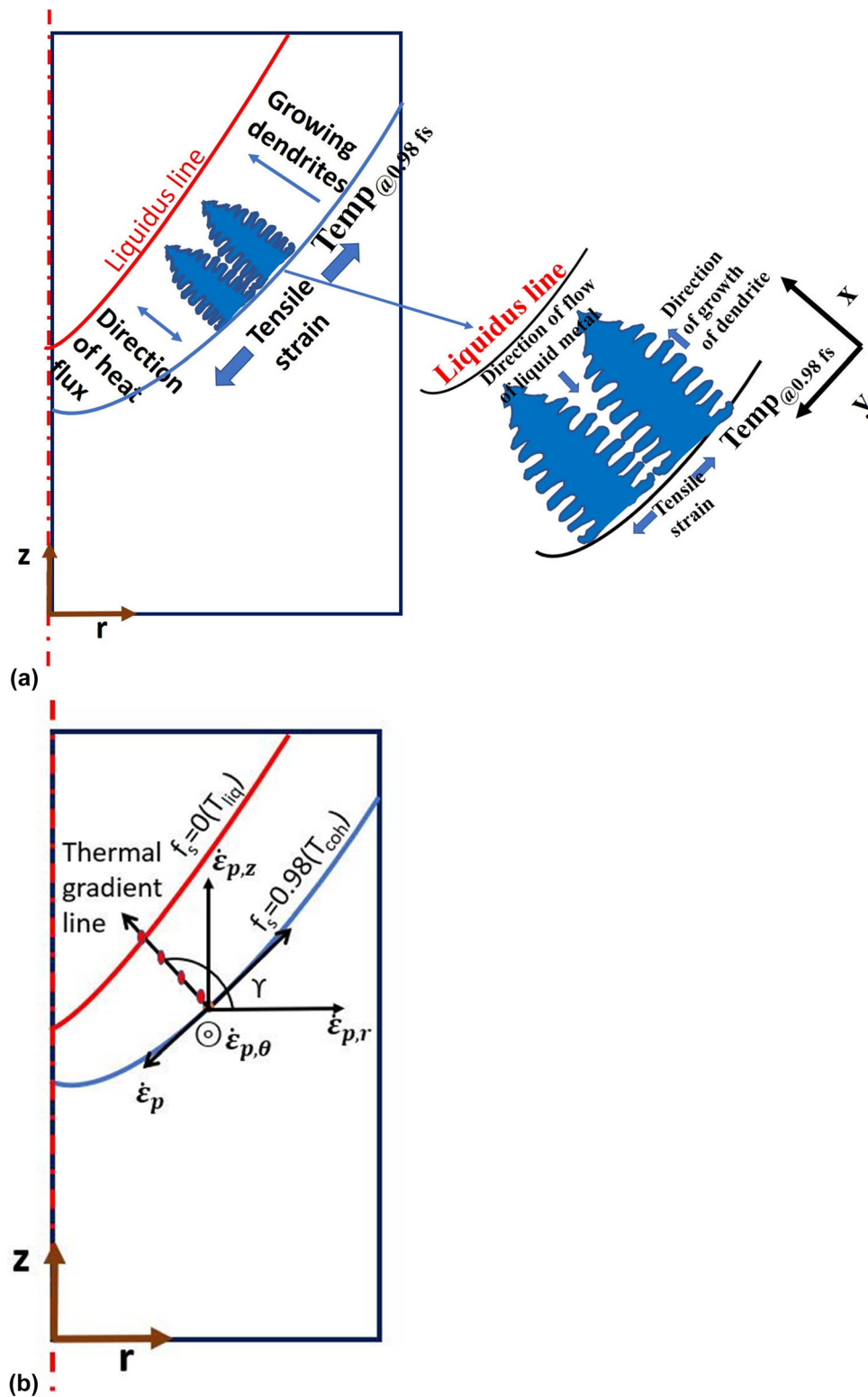


**Fig. 6** Schematic representing (a) growing columnar dendrites subjected to tensile strain, (b) three components of strain rate along with the thermal gradient

temperature ( $\frac{dT}{dt}$ ) in the mushy zone required for calculating depression pressure are extracted by suitable interpolation of nodal values from DC casting simulation.

For any desired location in the billet, the following procedure is adopted for calculating depression pressure. From

temperature history of any particular node, the time instant at which nodal temperature reaches the temperature corresponding to critical solid fraction ( $f_s=0.98$ ) is determined. At that instant of time, direction of thermal gradient is determined by plotting line perpendicular to isotherm passing through that



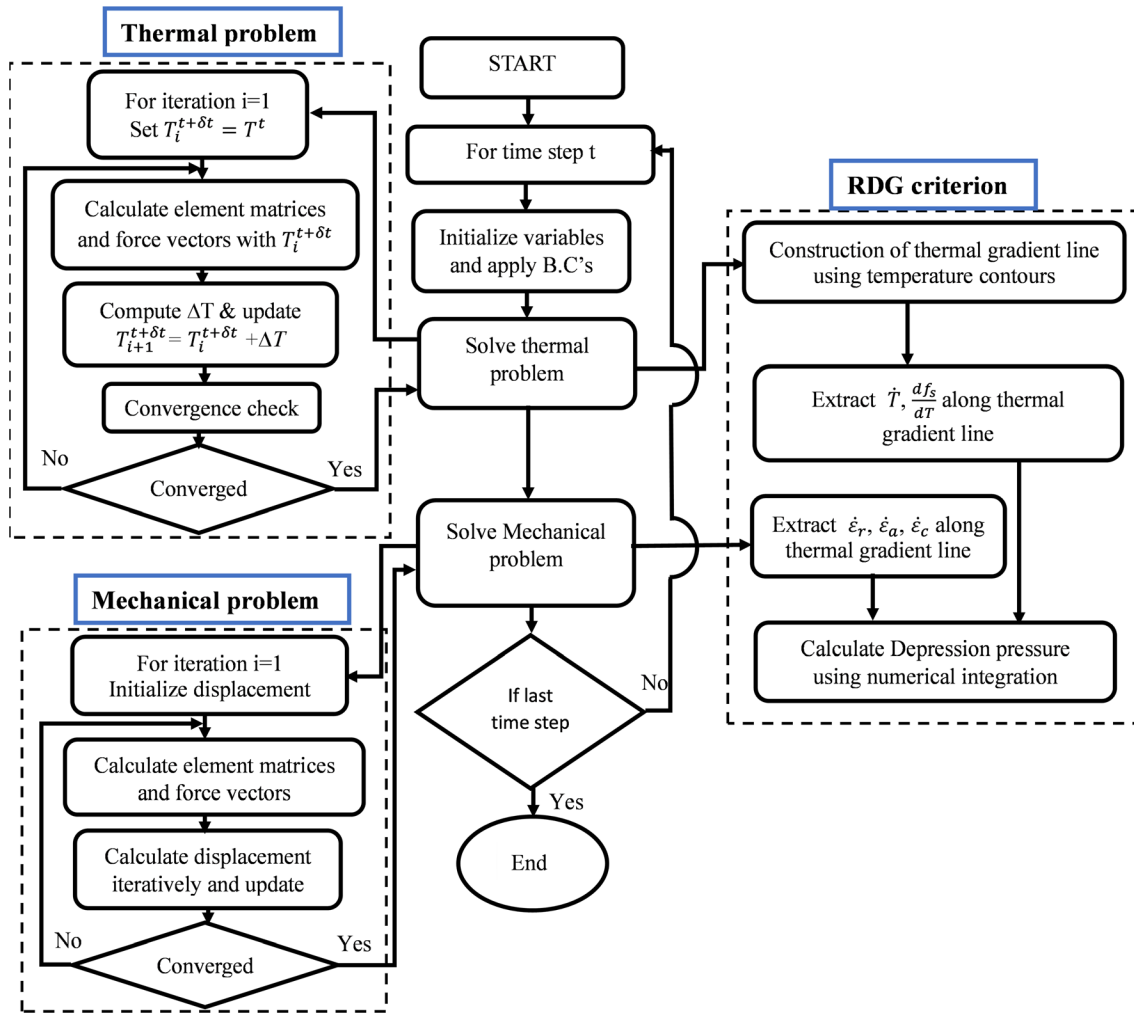


Fig. 7 Flowchart of thermo-mechanical modeling and RDG criterion

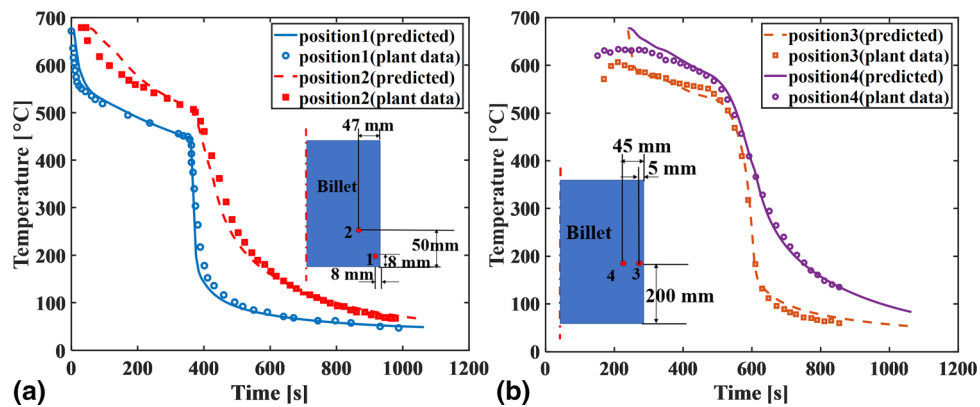


Fig. 8 Temperature profiles comparison at (a) positions 1 and 2, (b) positions 3 and 4

node. This thermal gradient line indicates the direction of heat flux which is the path of integration in Eq 15. Values of  $\dot{\epsilon}_p, f_s, \frac{df_s}{dT}, \frac{dT}{dt}$  along the integration path at the intersection points of element faces/edges are determined by suitable interpolation of nodal values.

Depression pressure is then calculated using trapezoidal rule reported by Hao et al. (Ref 10) at various locations in the billet.

The flowchart in Fig. 7 summarizes the algorithm used for thermo-mechanical modeling and studying hot cracking sensitivity using RDG criterion.

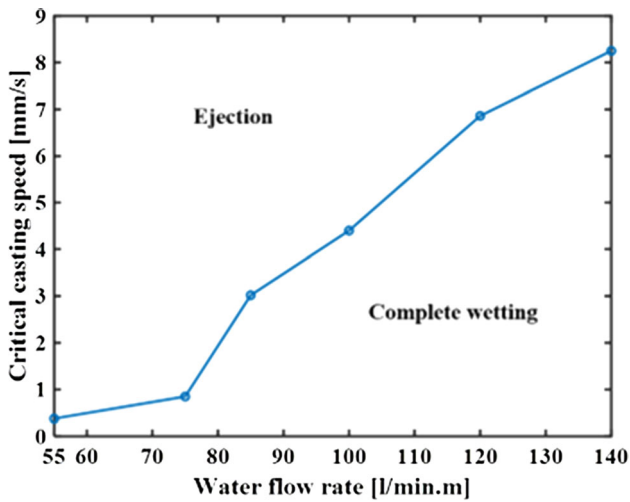


Fig. 9 Critical casting speed for various water flow rates

### 3. Results

Transient heat conduction equation (Eq 1) is solved for computational domain in Fig. 2, using boundary conditions discussed in section 2.1, 2.2. Temperature profiles in critical regions of the billet during the DC casting of AZ31 alloy are studied. The height of the mold is assumed as 300 mm. The impingement zone length is 15.8 mm for a water flow rate of 85 l/(min.m). Water flow rate is expressed in terms of volumetric flow rate/perimeter. The casting speed is 0.847 mm/s. Figure 8 compares numerically predicted temperature profiles with temperature measurements from different thermocouple locations in the billet during plant trials conducted by Hao et al. (Ref 26)

These locations are taken as:

- Position 1 (8 mm from the billet surface, 8 mm above the bottom block)
- Position 2 (47 mm from the billet surface, 50 mm above the bottom block)
- Position 3 (5 mm from the billet surface, 200 mm above the bottom block)
- Position 4 (45 mm from the billet surface, 200 mm above the bottom block).

There is a good agreement between predicted temperatures and measured plant data from thermocouples at all four locations. The surface temperature (position 1) drops to approximately 447 °C at the mold exit (~ 360 s). Below mold exit, the water directly strikes the surface. As the surface temperature in the impingement zone is less than Leidenfrost temperature, heat transfer occurs in transition/nucleate boiling zone due to the absence of film boiling. This causes surface temperature to drop quickly. At the end of impingement zone (~ 376 s), the surface temperature is 200 °C. This low surface temperature at the start of free-falling zone allows water to be intact with the surface which further decreases the temperature. Similar temperature profile is observed for other surface point (position 3) as shown in Fig. 8(b). Locations away from surface and toward the center (position 2 and 4) also show similar trend at higher temperatures.

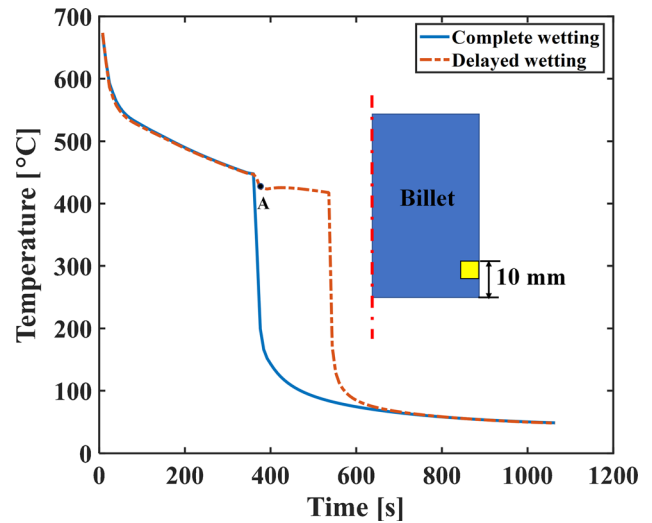


Fig. 10 Comparison of Temperature profiles for complete wetting and delayed wetting

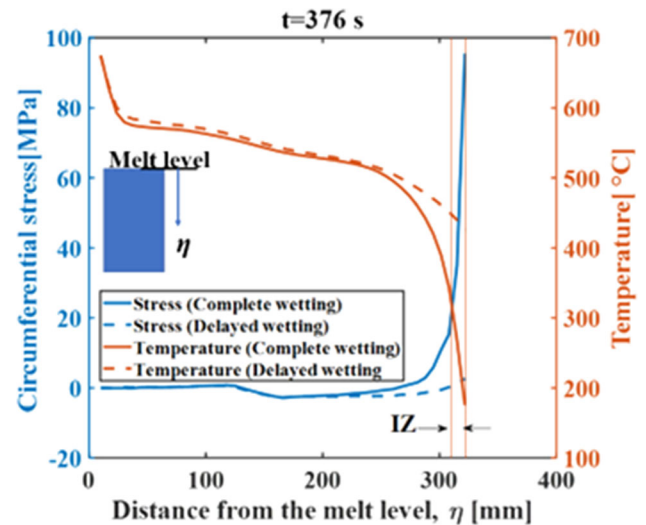
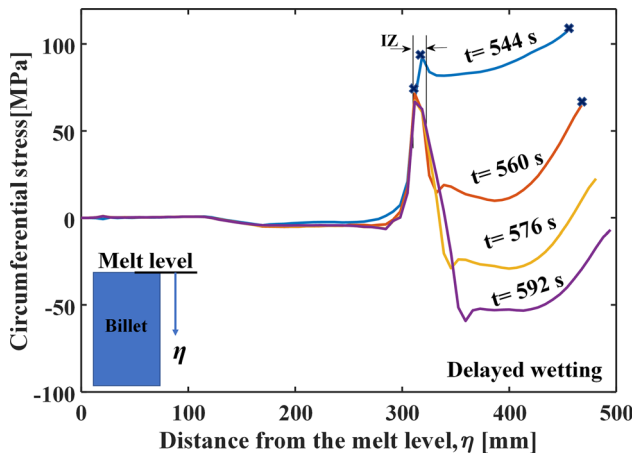


Fig. 11 Evolution of circumferential stress at the end of impingement zone for complete and delayed wetting cases

As discussed in Sect. 1, water ejection occurs in FFZ, if the surface temperature is above Leidenfrost temperature. The surface temperature in the FFZ is highly dependent on water flow rate and casting speed. To investigate the influence of water flow rate and casting speed, multiple simulations have been performed with different water flow rates and casting speeds. Figure 9 shows the relation between the casting speed and water flow rate. For a given flow rate, there exists a critical casting speed above which water ejection takes place and below which complete wetting of the surface is observed.

Thermal stresses developed during DC casting are significantly influenced by water ejection phenomenon and are crucial in estimating hot tearing sensitivity. Evolution of thermal stresses and visco-plastic strains is studied in detail for two different cases based on critical casting speed in Fig. 9.

Case 1: Complete/immediate wetting in the FFZ with flow rate of 85 l/(min.m) and casting speed of 0.847 mm/s.



**Fig. 12** Evolution of circumferential stress at various instances for delayed wetting

Case 2: Delayed wetting (ejection followed by rewetting in the FFZ) with flow rate of 55 l/(min m) and casting speed of 0.847 mm/s.

Figure 10 depicts temperature profiles of surface point located close to bottom block for cases of complete wetting and ejection. In case of complete wetting, surface temperature of billet at the mold exit (447 °C) is below Leidenfrost temperature. Therefore, film boiling is absent and water completely wets the billet surface. This results in rapid decrease in temperature. The presence of water in FFZ further reduces the temperature. However, in case of delayed wetting, surface temperature is still above Leidenfrost temperature at the impingement region due to reduced water flow rate. This causes film boiling with reduced heat transfer in this zone resulting in surface temperature of ~ 420 °C at the end of impingement zone corresponding to point A in Fig. 10. Since this is higher than the Leidenfrost temperature, film boiling occurs in free-falling zone. At this instant, water ejects from billet surface resulting in slow cooling and delay in temperature drop. Surface temperature remains higher for certain extended period of time. At ~ 536 s, temperature drops below rewetting temperature causing a steep temperature drop due to rewetting.

Further, the influence of water ejection and delayed wetting behavior on the evolution of stress profiles is studied. As circumferential stress can open up cracks in both radial and axial directions, evolution of the same is analyzed for both complete and delayed wetting cases. For the sake of convenience, stress profiles are discussed zone-wise. Figure 11 shows the variation of circumferential stress on billet surface with increasing distance from the melt level at the end of impingement zone (Point A corresponding to ~ 376 s in Fig. 10). For complete wetting case, circumferential stress reaches a peak value of 97 MPa at the end of impingement zone due to very high temperature drop (~ 200 °C). However, in delayed wetting case, stresses do not rise in impingement zone because of negligible temperature drop.

Figure 12 presents variation of circumferential stress on billet surface with increasing distance from melt level for the delayed wetting case. These stress profiles correspond to different instants after rewetting (i.e., after ~ 536 s). Immediately after rewetting, tensile stresses are observed on the surface below the rewetting point. As the wetting front propagates, nature of stresses below the rewetting point changes into

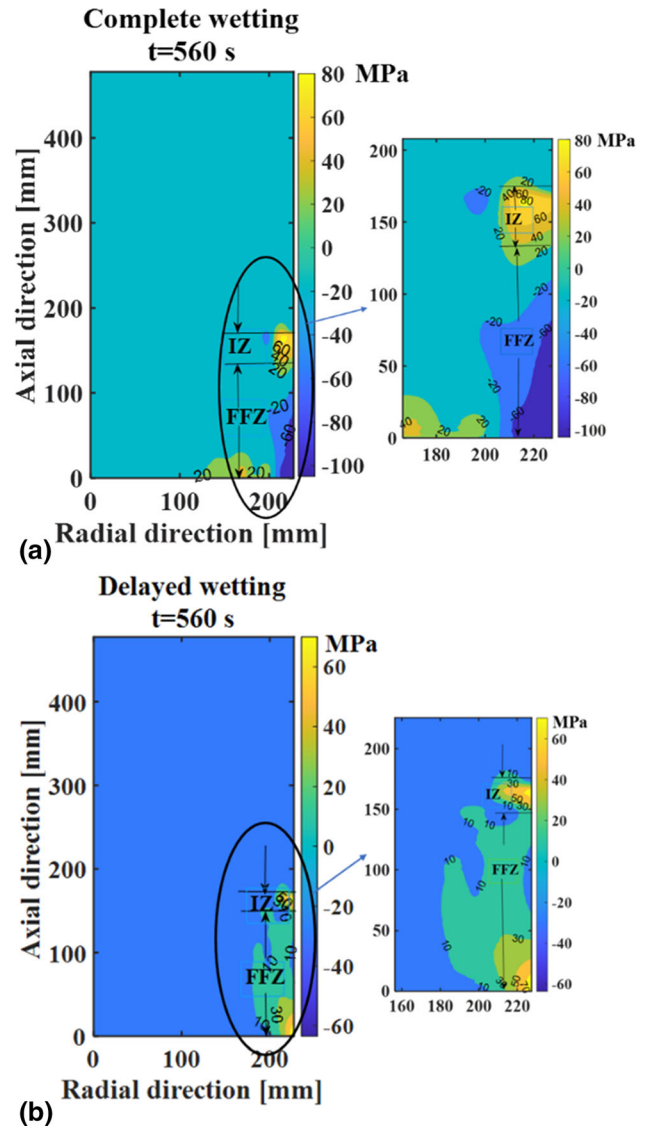
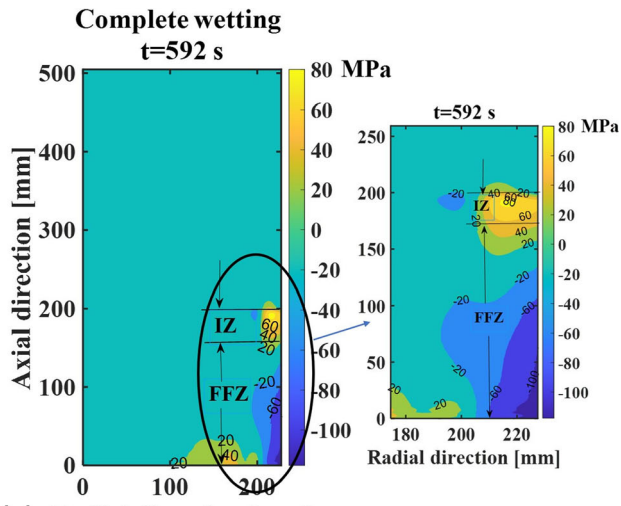


**Fig. 13** Circumferential stress contours ~ at 560 s (a) for complete wetting and (b) delayed wetting (immediately after rewetting)

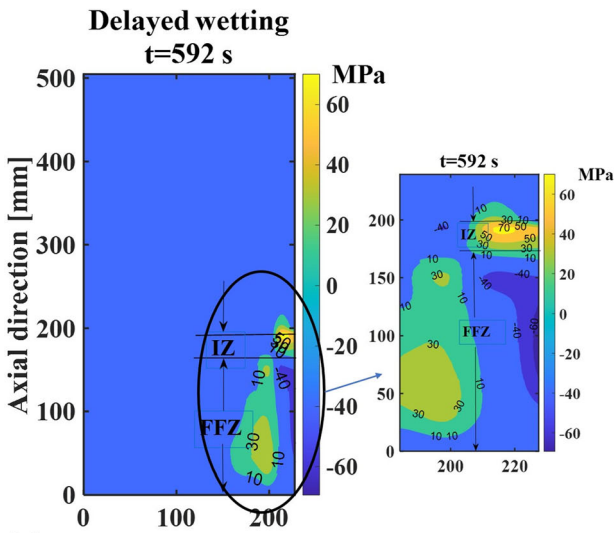
compressive. At ~ 544 s (immediately after rewetting), stresses are tensile over the entire billet surface with higher stresses close to the bottom block than the impingement zone. At ~ 576 s, the stress below the wetting front is entirely compressive. Similar behavior is observed till the end of casting process. Figure 13 compares circumferential stress contours at an instance after rewetting (~ 560 s) for complete and delayed wetting cases. Tensile stresses are observed in the impingement zone for both cases. However, at the bottom of billet, stresses change to compressive for complete wetting and remain tensile in case of delayed wetting. As wetting front progresses (~ 592 s), nature of circumferential stresses changes to compressive in case of delayed wetting, as shown in Fig. 14.

Evolution of stresses and strains for both complete and delayed wetting cases are analyzed for different material points that correspond to peak stress in impingement zone. Locations of 165.84 mm and 85 mm from bottom of the billet are selected for delayed and complete wetting cases, respectively.

For complete wetting case, Fig. 15(a) shows stress profiles at two positions: P at center and Q at surface. The positions at a



(a) Radial direction [mm]

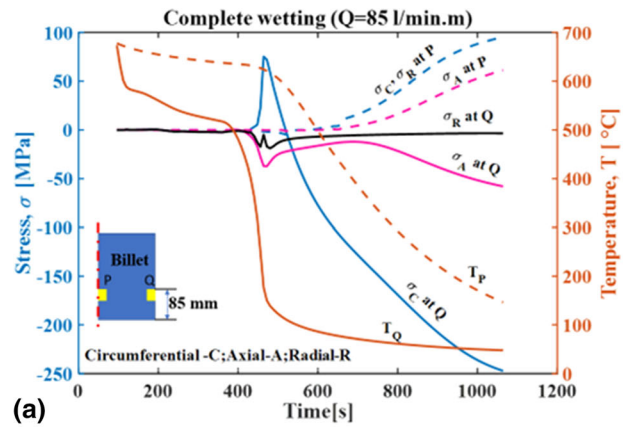


(b) Radial direction [mm]

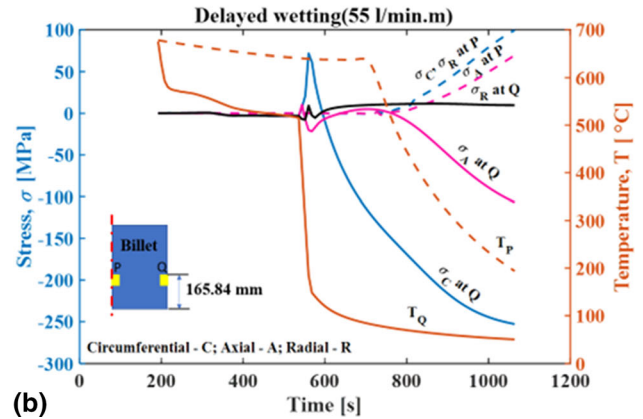
Fig. 14 Circumferential stress contours  $\sim$  at 592 s (a) for complete wetting and (b) delayed wetting (certain instance after rewetting)

distance of 85 mm from the bottom of the billet are selected to avoid the effect of fixed boundary conditions at the bottom region. Temperature profiles are also depicted to understand the influence of temperature on evolution of all the three stress components, i.e., circumferential, radial and axial.

Due to differences in the cooling behavior experienced at center and surface of the billet, variation in stress profiles is observed at both locations. At the surface, circumferential stress is negligible in the mold region (up to 424 s) which increases to peak value of 75 MPa ( $\sim$  464 s) due to sudden drop in temperature at mold exit. With further cooling, the nature of stress gradually changes to compressive. In contrast, circumferential stress in the mold region is almost negligible at the center. It increases gradually with further increase in cooling reaching a maximum value of 95 MPa at the end of casting ( $\sim$  1064 s). At surface, axial stresses are negligible until the mold exit beyond which nature of stresses change to compressive. The center experiences negligible stress until 600 s beyond which they are tensile. Radial stress is negligible at the



(a)



(b)

Fig. 15 Comparison of three stress components at two locations (center and surface) for complete and delayed wetting

surface. Because of symmetry, circumferential and radial components are equal at the center.

Stress profiles for delayed wetting case are shown in Fig. 15(b). As the surface temperature of the billet is higher than the Leidenfrost temperature at the impingement point, immediate wetting of the billet is not observed. At 536 s, sudden temperature drop is observed as the billet temperature is less than rewetting temperature. Correspondingly, circumferential stress increases rapidly at the surface. After attaining a peak value of 71.54 MPa, there is a gradual change in nature of stress to compressive similar to complete wetting case. Axial and radial stress profiles are also similar to those observed in the case of complete wetting. At center, all the three stress components are tensile and profiles are similar to complete wetting case.

In Fig. 16(a), all three visco-plastic strain components are plotted along with temperature profiles for two locations (center and surface) at 85 mm from the bottom. At surface, circumferential and axial strains are tensile and radial strain is compressive within the mold. At the mold exit, the temperature drop in the impingement zone causes further increase in the circumferential and axial strains. After certain time, all surface strain profiles are constant due to negligible change in the temperature ( $\sim$  after 528 s). At the center, no strains are observed within the mold as temperature is almost constant in the mold. At the mold exit, due to the cooling in the impingement zone, temperature gradually decreases resulting in gradual increase in strains. In Fig. 16(a), as the temperature at

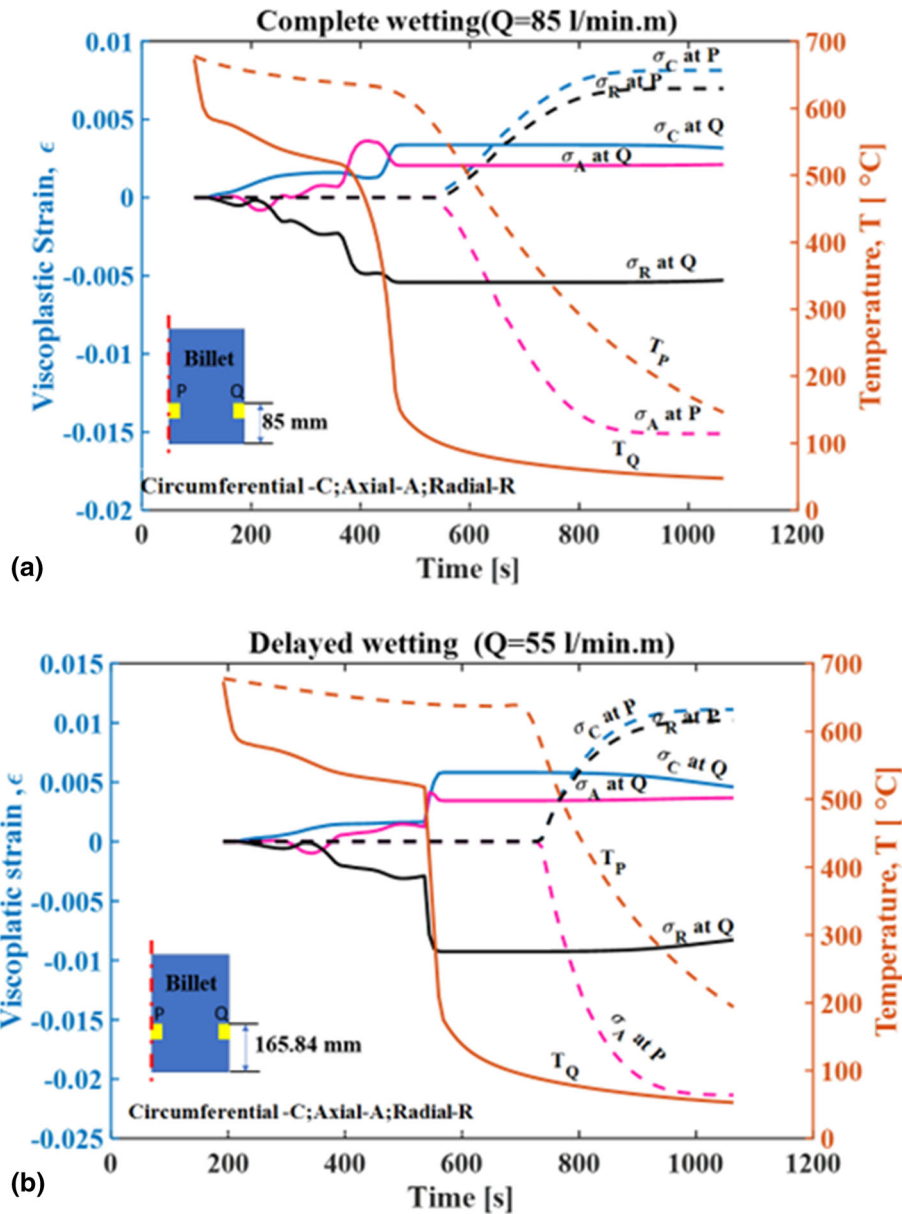


Fig. 16 Comparison of three strain components at two locations (center and surface) for complete and delayed wetting

the center drops below the coherency temperature beyond 528 s, tensile strains are observed in circumferential and radial directions. Three visco-plastic strain components for the delayed wetting case are plotted in Fig. 16(b). The attainment of tensile strain at the center is delayed compared to complete wetting. The steady-state tensile strain in the delayed wetting case ( $\epsilon = 0.011$ ) is higher than complete wetting case ( $\epsilon = 0.008$ ).

Among the various hot tearing criteria studied by Suyitno et al. (Ref 21) and Song et al. (Ref 23), RDG criterion is reported to precisely predict the formation of hot tears as it takes both the thermal and mechanical effects into consideration. As detailed in Sect. 2.3, depression pressure is calculated at the various locations in the billet for assessing the locations susceptible to the formation of hot tears using RDG criterion. In Fig. 17, total depression pressure in both the cases is highest at the bottom of the billet and gradually decreases along the height the billet. In case of delayed wetting, peak depression pressure

is  $\sim 480 \text{ kPa}$  compared to  $\sim 375 \text{ kPa}$  in case of complete wetting. Therefore, for billet casting, regions close to bottom block are more prone to hot tears.

The total depression pressure variation along the radial direction at different heights from the bottom of the billet for both the cases is plotted in Fig. 18(a) and (b). Depression pressure is highest near the center and gradually reduces in the radial direction. In complete wetting (Fig. 18a), depression pressure of 325 kPa is observed near the center at a height of 30 mm from the bottom, which reduces to 85 kPa moving toward the surface. Depression pressure is highest for location 30 mm compared to the other locations from the bottom of the billet. However, in case of delayed wetting, the magnitude of depression pressure across the radial direction for different heights is higher compared to complete wetting as shown in Fig. 18(b).

Further, the influence of casting speed on hot cracking sensitivity is studied at three casting speeds ( $V$ ), i.e., 50, 65 and

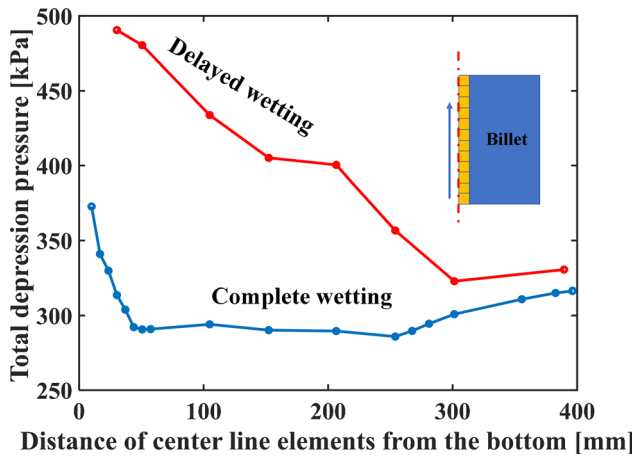


Fig. 17 Variation of depression pressure along the centerline of the billet for complete wetting and delayed wetting

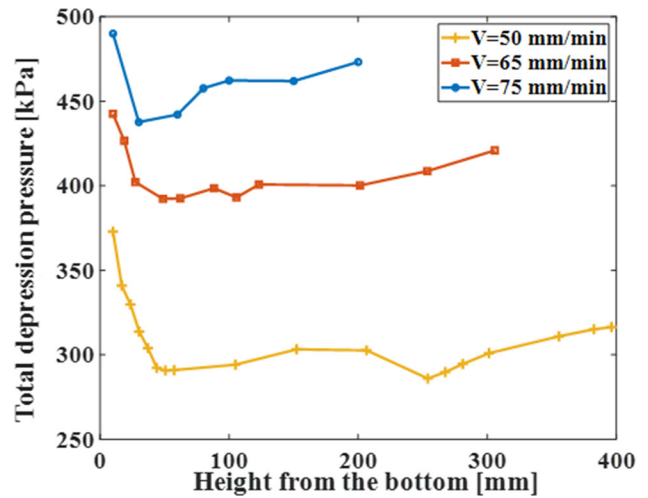


Fig. 19 Depression pressure variation along the centerline from the bottom of the billet for three casting speeds

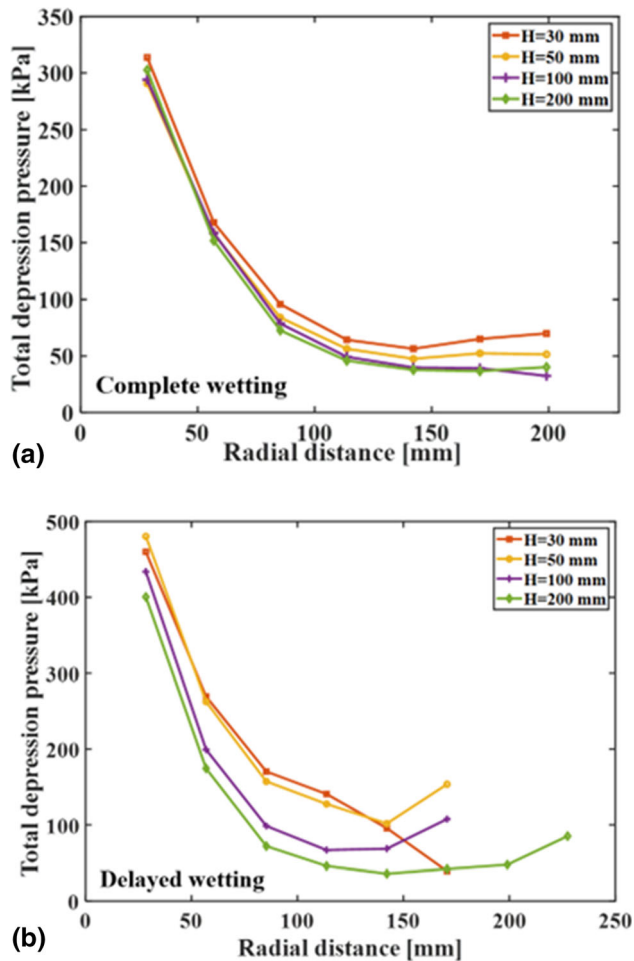


Fig. 18 Depression pressure variation along the radial direction at different heights from the bottom of the billet for (a) complete wetting, (b) delayed wetting

75 mm/min, for a constant flow rate of 85 l/(min.m) using RDG criterion. Figure 19 shows the variation of depression pressure near the center along the height of the billet for the

three casting speeds. For a given casting speed, maximum depression pressure is observed near the bottom of the billet which further decreases with increasing distance from the bottom of the billet. This behavior is in line with the studies reported on aluminum alloys by Suyitno et al. (Ref 21) and Drezet and Rappaz (Ref 30). For casting speeds of 50 and 75 mm/min, peak depression pressures of 370 and 490 kPa, respectively, are observed near the centerline closer to the bottom of the billet. With increasing distance from the bottom, depression pressure decreases and finally reaches 310 and 460 kPa at 400 and 200 mm from bottom of the billet, respectively. As casting speed increases, depression pressure increases indicating higher sensitivity to cracking at high speeds. For all the three casting speeds, near to the centerline, bottom region of the billet is highly prone to hot cracking.

Based on the above results, for complete wetting case, the absence of film boiling causes immediate wetting in the impingement zone cooling the entire billet. This results in peak tensile stresses at the impingement zone and compressive stresses below this region as represented in schematic in Fig. 20. In the delayed wetting case, immediately after rewetting, high tensile stresses are observed near the bottom of the billet. This increases the tendency of the billet to surface cracks. As the wetting front propagates and decreases the surface temperature of the billet, compressive stresses are developed on the surface. Depression pressures calculated from RDG criterion also indicate that regions close to center and bottom of the billet are more susceptible to hot tearing in both cases. The study on the effect of casting speed on hot tearing susceptibility indicates that an increase in casting speed increases the risk of hot tearing.

#### 4. Summary and Conclusions

The occurrence of water ejection is more critical in DC casting. It causes the cast ingot/billet temperature to remain higher for longer times. This may initiate hot tears in the mushy zone. In this work, thermo-mechanical analysis of magnesium

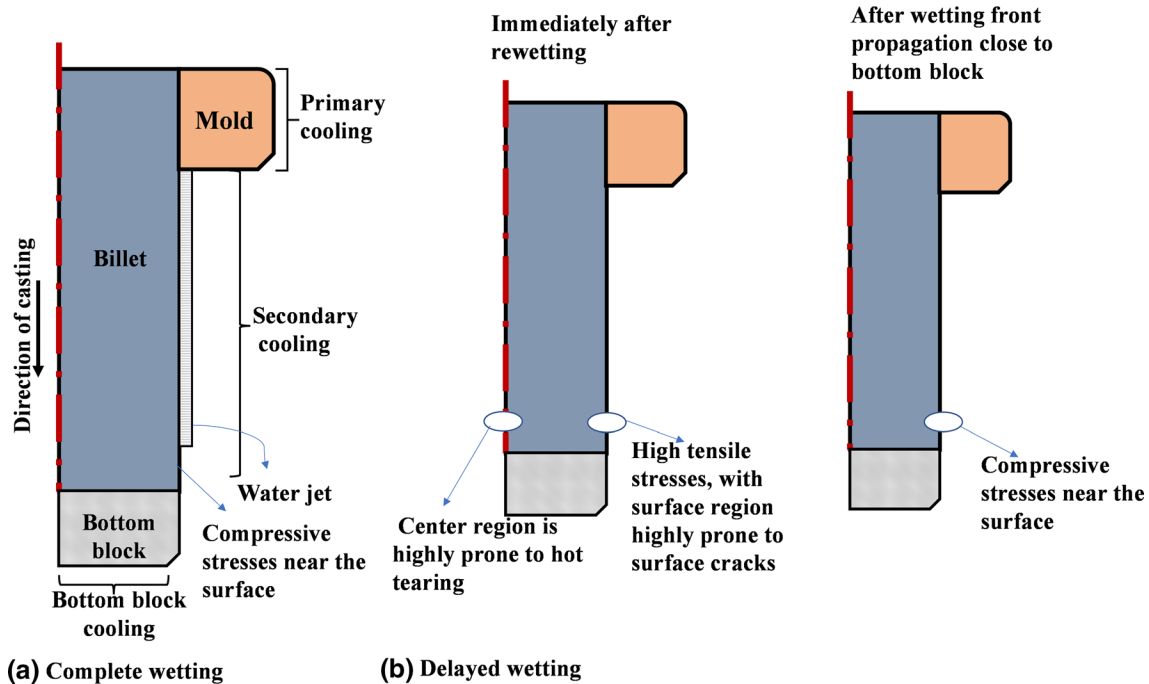


**Fig. 20** Schematic representing critical zones for areas prone to hot cracking (a) complete wetting, (b) delayed wetting

alloy DC casting was performed to assess the influence of water ejection on thermal stress and hot tears. Critical casting speed which defines the speed above which complete ejection always occurs and below which complete wetting takes place was calculated for various cooling water flow rates. Thermal stress profiles were estimated for two different cases: complete wetting and delayed wetting (ejection followed by wetting). Further, hot cracking sensitivity studies were carried out for both cases using RDG criterion. From this study, the following observations can be made.

- During the delayed wetting situation, peak circumferential stress was observed at the bottom of the billet in contrast to that occurring at the impingement point in case of complete wetting. Also, stresses near the bottom block region were high during this period and may cause hot tearing. After rewetting, further cooling due to wetting front propagation induced compressive stress at the surface.
- For both complete and delayed wetting, depression pressure decreased with distance from the center in the radial direction, indicating that the center of the billet is sensitive to hot tearing compared to billet surface. However, magnitudes of depression pressure were higher for delayed wetting case.
- Along the centerline, depression pressure was high near the bottom of the billet and decreased further when moving away from the bottom. This indicates that the locations closer to the bottom of the billet were more prone to hot tearing.
- The influence of casting speed on hot cracking sensitivity was studied. Higher casting speeds increased the billet's susceptibility to hot tearing as calculated depression pressures were increasing with casting speed.

## References

1. E. Caron and M.A. Wells, Secondary Cooling in the Direct-Chill Casting of Magnesium Alloy AZ31, *Metall. Mater. Trans. B Process Metall. Mater. Process Sci.*, 2009, **40**(4), p 585–595.
2. JF Grandfield, Direct Chill Casting of Magnesium Extrusion Billet and Rolling Slab. Adv Wrought Magnes Alloy Fundam Process Prop Appl. 2012, p 229-271
3. E. Caron and M.A. Wells, Film Boiling and Water Film Ejection in the Secondary Cooling Zone of the Direct-Chill Casting Process, *Metall. Mater. Trans. B Process Metall. Mater. Process Sci.*, 2012, **43**(1), p 155–162.
4. G.A. Kulkarni, Local Heat Transfer and Stress Analysis of Direct Chill Casting Process, Ph.D Thesis, Ottovon Guericke University, Magdenburg, 2019, <https://doi.org/10.25673/13468>
5. P.V. Sai Divya, P.K. Penumakala and A.K. Nallathambi, Influence of Secondary Cooling Strategies on Thermal Gradients in the Direct Chill Casting of Magnesium Alloys, *J. Therm. Anal. Calorim.*, 2022, **147**(1), p 203–218. <https://doi.org/10.1007/s10973-020-10235-7>
6. E. Caron and M.A. Wells, Effect of Advanced Cooling Front (ACF) Phenomena on Film Boiling and Transition Boiling Regimes in the Secondary Cooling Zone during the Direct-Chill Casting of Aluminum Alloys, *Mater. Sci. Forum*, 2006, **519–521**, p 1687–1692.
7. S. Bolduc and L.I. Kiss, Sensitivity Study of the Influence of the Water Boiling Parameters on Aluminum Semi-Continuous DC Casting, *Int. J. Therm. Sci.*, 2020, **151**, p 106276.
8. J. Sengupta, S.L. Cockcroft, D. Maijer, M.A. Wells and A. Larouche, The Effect of Water Ejection and Water Incursion on the Evolution of Thermal Field during the Start-up Phase of the Direct Chill Casting Process, *J. Light Met.*, 2002, **2**(3), p 137–148.
9. J. Sengupta, S.L. Cockcroft, D.M. Maijer, M.A. Wells and A. Larouche, On the Development of a Three-Dimensional Transient Thermal Model to Predict Ingot Cooling Behavior during the Start-up Phase of the Direct Chill-Casting Process for an AA5182 Aluminum Alloy Ingot, *Metall. Mater. Trans. B Process Metall. Mater. Process Sci.*, 2004, **35**(3), p 523–540.
10. H. Hao, D.M. Maijer, M.A. Wells, A. Phillion and S.L. Cockcroft, Modeling the Stress-Strain Behavior and Hot Tearing during Direct

- Chill Casting of an AZ31 Magnesium Billet, *Metall. Mater. Trans. A Phys. Metall. Mater. Sci.*, 2010, **41**(8), p 2067–2077.
11. M. Turski, J.F. Grandfield, T. Wilks, B. Davis, R. Delorme, and K. Cho, Computer Modeling of DC Casting Magnesium Alloy WE43 Rolling Slabs, *Essent. Readings Magnes. Technol.*, 2014, p 457–462. doi:<https://doi.org/10.1002/9781118859803.ch74>
  12. J.M. Drezet and T. Pirling, Influence of a Wiper on Residual Stresses in AA7050 Rolling Plate Ingots, *J. Mater. Process. Technol.*, 2014, **214**(7), p 1372–1378. <https://doi.org/10.1016/j.jmatprotec.2014.02.011>
  13. H. Hongjun, Z. Dingfei and Y. MingBo, Numerical Simulation of Thermal Stress in Cast Billets Made of AZ31 Magnesium Alloy during Direct-Chill Casting, *J. Manuf. Process.*, 2008, **10**(2), p 82–88. <http://doi.org/10.1016/j.jmapro.2008.12.002>
  14. Suyitno, W.H. Kool and L. Katgerman, Finite Element Method Simulation of Mushy Zone Behavior during Direct-Chill Casting of an Al-45 Pct Cu Alloy, *Metall. Mater. Trans. A*, 2004, **35**(9), p 2917–2926
  15. C. Menapace, L. Fioretta, G. Straffelini, L. Canevari and S. Sannicola, Microstructural Characterisation and Hot-Deformation Behaviour of AA6082 Al Alloy Produced by Low-Frequency Electromagnetic Casting, *J. Mater. Eng. Perform.*, 2020, **29**, p 2667–2678. <https://doi.org/10.1007/s11665-020-04763-4>
  16. S. Ramasamy, Influence of Water Ejection on Thermal Stresses in Direct Chill Casting, Master Thesis, Ottovon Guericke University, Magdenburg, 2018
  17. J. Sengupta, S.L. Cockcroft, D.M. Maijer and A. Larouche, Quantification of Temperature, Stress, and Strain Fields during the Start-up Phase of Direct Chill Casting Process by Using a 3D Fully Coupled Thermal and Stress Model for AA5182 Ingots, *Mater. Sci. Eng. A*, 2005, **397**(1–2), p 157–177.
  18. J.F. Grandfield, D.G. Eskin and I. Bainbridge, *Direct-Chill Casting of Light Alloys*, 1st ed. The Minerals Metals Materials society, US, 2013, p 173–204
  19. D.G. Eskin, Suyitno, and L. Katgerman, Mechanical Properties in the Semi-Solid State and Hot Tearing of Aluminium Alloys, *Prog Mater Sci*, 2004, **49**(5):629–711
  20. A.N.S.S. Swain, S. Ganguly, A. Sengupta, E.Z. Chacko, S. Dhakate and P.K. Pandey, Investigation of Corner Cracks in Continuous Casting Billet Using Thermomechanical Model and Plant Measurements, *Met. Mater. Int.*, 2022 <https://doi.org/10.1007/s12540-021-01135-y>
  21. Suyitno, W.H. Kool, and L. Katgerman, Hot Tearing Criteria Evaluation for Direct-Chill Casting of an Al-4.5 Pct Cu Alloy, *Metall. Mater. Trans. A Phys. Metall. Mater. Sci.*, 2005, **36**(6):1537–1546
  22. L. Bichler and C. Ravindran, Investigations on the Stress and Strain Evolution in AZ91D Magnesium Alloy Castings During Hot Tearing, *J. Mater. Eng. Perform.*, 2015, **24**, p 2208–2218. <https://doi.org/10.1007/s11665-015-1454-9>
  23. J. Song, F. Pan, B. Jiang, A. Atrens, M.X. Zhang and Y. Lu, A Review on Hot Tearing of Magnesium Alloys, *J. Magnes. Alloy.*, 2016, **4**(3), p 151–172. <https://doi.org/10.1016/j.jma.2016.08.003>
  24. M. Rappaz, J.M. Drezet and M. Gremaud, A New Hot-Tearing Criterion, *Metall. Mater. Trans. A Phys. Metall. Mater. Sci.*, 1999, **30**(2), p 449–455.
  25. P. Pavan Kumar, A.K. Nallathambi, E. Specht and A. Bertram, Mechanical Behavior of Mushy Zone in DC Casting Using a Viscoplastic Material Model, *Tech Mech*, 2012, **32**(2), p 342–357.
  26. H. Hao, D.M. Maijer, M.A. Wells, S.L. Cockcroft, D. Sediako and S. Hibbins, Development and Validation of a Thermal Model of the Direct Chill Casting of AZ31 Magnesium Billets, *Metall. Mater. Trans. A Phys. Metall. Mater. Sci.*, 2004, **35**(12), p 3843–3854.
  27. K. Hu, A.B. Phillion, D.M. Maijer and S.L. Cockcroft, Constitutive Behavior of As-Cast Magnesium Alloy Mg-Al3-Zn1 in the Semi-Solid State, *Scr. Mater. Acta Materialia Inc*, 2009, **60**(6), p 427–430. <https://doi.org/10.1016/j.scriptamat.2008.11.011>
  28. J. Li and X. Xia, Modeling High Temperature Deformation Behavior of Large-Scaled Mg-Al-Zn Magnesium Alloy Fabricated by Semi-Continuous Casting, *J. Mater. Eng. Perform.*, 2015, **24**(9), p 3539–3548.
  29. P.V. Sai Divya, P.K. Penumakala and A.K. Nallathambi, Effect of Wiper on Thermal Stresses During Direct Chill Casting of Magnesium Alloy, *Mater Today Proc.*, 2019, **46**, p 9316–9322. <https://doi.org/10.1016/j.matpr.2020.02.773>
  30. J.M. Drezet and M. Rappaz, Prediction of Hot Tears in DC-Cast Aluminum Billets, *Light Met. Proc. Sess. TMS Annu. Meet. (Warrendale, Pennsylvania)*, 2001, p 887–893

**Publisher's Note** Springer Nature remains neutral with regard to jurisdictional claims in published maps and institutional affiliations.

Springer Nature or its licensor (e.g. a society or other partner) holds exclusive rights to this article under a publishing agreement with the author(s) or other rightsholder(s); author self-archiving of the accepted manuscript version of this article is solely governed by the terms of such publishing agreement and applicable law.